Hindawi Publishing Corporation
Advances in Meteorology
Volume 2014, Article ID 584040, 16 pages
http://dx.doi.org/10.1155/2014/584040

Research Article

Relative Contribution of the Topographic Influence on the Triangle Approach for Evapotranspiration Estimation over Mountainous Areas

Xiaosong Zhao and Yuanbo Liu

State Key Laboratory of Lake Science and Environment, Nanjing Institute of Geography and Limnology, Chinese Academy of Sciences, Nanjing 210008, China

Correspondence should be addressed to Yuanbo Liu; ybliu@niglas.ac.cn

Received 10 June 2014; Revised 13 October 2014; Accepted 13 October 2014; Published 5 November 2014

Academic Editor: Hiroyuki Hashiguchi

Evapotranspiration (ET) is an important component of the water budget. Estimation ET through remote sensing over a mountainous terrain is typically obstructed by topographic effects. In this paper, topographic corrections were applied to ET estimates using the surface-air temperature difference-Normalized Difference Vegetation Index ($(T_s - T_a)$-NDVI) triangle method with MODIS data for the Taihu Basin in China. The effect of topography on ET was evaluated over an area with a complex terrain. After applying the topographic correction, the results indicate that the ET decreased with elevation and slope. The slope had a stronger impact on ET than the elevation, which caused the corrected ET to decrease by 90% from 6.8 mm day^{-1} to 0.6 mm day^{-1} for slopes over 50°. On average, the corrected ET decreased by 10.4% and 32.1% for north- and south-facing slopes, respectively. The ET corrected using the triangle method strongly depended on the evaporative fraction correction, which can mainly be attributed to the surface temperature correction. We conclude that a topographic correction is necessary when the triangle method is applied to areas with a complex terrain.

1. Introduction

Evapotranspiration (ET), which includes water evaporation from soil surfaces and vegetation transpiration, is an important variable in water and energy balances on the Earth's surface. Understanding the spatial distribution of ET is essential for many environmental monitoring applications, including water resource management, agricultural efficiency, global vegetation analysis, climate dynamics, and ecological applications [1–3]. Although the ET may be accurately estimated from detailed ground observations, direct field measurements only represent local scales over a few hundred square meters. It is difficult to conduct ground observations on a large scale due to the high cost and spatial range discontinuities [4].

Remote sensing technology can provide land surface parameters, such as surface temperature, albedo, and vegetation indices, which are indispensable to remote sensing-based methods that estimate the area-averaged ET on a regional scale [5]. Several remote sensing-based methods with varying complexities have been developed to map ET at various spatial scales. Typical examples include the simplified empirical method [6], the surface energy balance-based single- or dual-source models [7, 8], the spatial contexture information-based surface temperature-vegetation index (T_s-VI) triangular or trapezoidal methods [9, 10], and data assimilation techniques [11].

Among these methods, the T_s-VI triangle method is widely accepted for its simplicity. The method was first introduced by Price [12], who used the spatial contexture of surface radiant temperature and fractional vegetation cover to estimate ET in the Southern Great Plains, USA. Thereafter, the triangle method was improved and successfully applied to monitor soil moisture water content and droughts [12–17] in addition to ET [18–20]. Notably, Jiang and Islam [10, 19] used the well-known Priestley-Taylor equation [21] to estimate ET using a triangular relationship constructed for remotely sensed T_s versus the Normalized Difference Vegetation Index

(NDVI). This relationship was further developed with other VI, including the Enhanced Vegetation Index (EVI) and fractional vegetation cover (Fr), using various remote-sensing data [5, 22–26].

The triangle method implicitly requires a flat surface and a large number of satellite pixels over an area containing a wide range of soil moisture and fractional vegetation cover [4]. Elevation, terrain slope, and aspect angles variations can interact with the satellite-viewing geometry to produce biases in the land surface parameters retrieved [27]. The biases in the relevant parameters may induce errors in the subsequent ET retrieval. While a large fraction of the Earth's surface consists of mountainous areas, few satellite products are corrected for terrain-induced angular effects. Gao et al. [28] evaluated the spatial variation in daily ET for a complex terrain based on the surface energy balance algorithm for land (SEBAL) but did not address ET retrieval errors related to topographic effects. To date, the extent to which the terrain affects ET retrieval using the triangle method and the parameters responsible for the terrain-induced errors are unknown. Clarifying the uncertainties will enhance our confidence using satellite data over rugged areas.

The aim of this study was to address the effects of topography on evapotranspiration estimates from remote-sensing data using the triangle method. Thus, topographic correction techniques were applied to correct the parameters relevant to ET over a complex terrain. We compared the ET estimated with and without topographic corrections to quantify the influence on ET in mountainous areas. Finally, suggestions were proposed for practical use of the triangle method using satellite products without topographic corrections.

2. Methodology

2.1. ET Retrieval Using the Triangle Method. The triangle relationship between the remotely sensed surface temperature and vegetation index can be applied to estimate ET using the following equation [19]:

$$\lambda \mathrm{ET} = \mathrm{EF}\left(R_n - G\right), \tag{1}$$

where λET denotes ET (W m^{-2}), R_n is the net radiation (W m^{-2}), and G is the soil heat flux (W m^{-2}). EF denotes the evaporative fraction (EF), which is defined as the ratio of ET to the available radiant energy ($R_n - G$):

$$\mathrm{EF} = \Phi \frac{\Delta}{\Delta + \gamma}, \tag{2}$$

where Δ is the slope of the saturated vapor pressure at the air temperature (T_a), γ is the psychrometric constant (hPa K^{-1}), and Φ is a parameter that accounts for aerodynamic and canopy resistances.

For the triangle method, the parameter Φ was calculated based on a triangular space using several types of expression, including a T_s-VI scatterplot, T_s-albedo scatterplot, and surface-air temperature difference versus VI scatterplot [4]. The T_s-VI triangle method requires a flat area [4], which yields large uncertainties when applied over areas with irregular topography. Because air temperature varies greatly over the screen, the surface-air temperature difference ($T_s - T_a$) is the true temperature variable for the triangle method over the topographic terrain [9, 10]. In this study, based on the surface-air temperature difference ($T_s - T_a$) versus the NDVI space, the upper and lower Φ for each NDVI interval were established, and we generated a linear interpolation for each NDVI interval between the lower and the highest ($T_s - T_a$). The Φ for a pixel at (NDVI$_i$, T_i) is as follows [19]:

$$\Phi = \frac{T_{i,\max} - T_i}{T_{i,\max} - T_{i,\min}} \left(\Phi_{i,\max} - \Phi_{i,\min}\right) + \Phi_{i,\min}. \tag{3}$$

The global minimum and maximum Φ are, respectively, $\Phi_{\min} = 0$ for the driest bare soil pixel and $\Phi_{\max} = 1.26$ for the pixel with dense vegetation and the largest NDVI. The $\Phi_{i,\min}$ was then linearly interpolated for each NDVI interval (NDVI$_i$) between $\Phi_{\min}$ and $\Phi_{\max}$, and the $\Phi_{i,\max}$ for each NDVI$_i$ was obtained from the lowest ($T_s - T_a$) pixel at the particular NDVI interval. The Φ_i value in each NDVI interval was interpolated between the lowest ($T_s - T_a$) pixel ($T_{i,\min}$, $\Phi_{i,\max}$) and highest ($T_s - T_a$) pixel ($T_{i,\max}$, $\Phi_{i,\min}$). Consequently, the Φ value for each pixel can be determined using the spatial context of the ($T_s - T_a$) and NDVI.

R_n is the net flux of four radiative components, including downward and upward shortwave radiation as well as downward and upward longwave radiation, which can be expressed as follows:

$$R_n = R_s^{\downarrow} - R_s^{\uparrow} + R_L^{\downarrow} - R_L^{\uparrow}, \tag{4a}$$

where $R_s^{\downarrow}$ and $R_s^{\uparrow}$ are the downward and upward shortwave radiation (W m^{-2}), respectively, and $R_L^{\downarrow}$ and $R_L^{\uparrow}$ are the downward and upward longwave radiation (W m^{-2}), respectively. Equivalently,

$$R_n = \left(1 - \rho\right) R_s^{\downarrow} + \sigma \varepsilon_a T_a^4 - \sigma \varepsilon_s T_s^4, \tag{4b}$$

where ρ is the surface albedo, ε_a is the emissivity of the air, ε_s is the surface emissivity, T_a is the air temperature (K) at the screen level, and σ is the Stefan-Boltzmann constant (5.67×10^{-8} W m^{-2} K^{-4}).

The soil heat flux (G) varies with the time of day, and it can be parameterized as a function of NDVI and R_n using the following equation [29]:

$$G = 0.583 \exp\left(-2.13\mathrm{NDVI}\right) R_n. \tag{5}$$

Instantaneous ET estimates are calculated at the satellite overpass time and then extrapolated to daily values by assuming a constant daytime evaporative fraction. The ET in a time series should be reconstructed based on ET retrieval for a clear day. In the Taihu watershed, the potential ET (based on Peman-Monteith equation) and daily ET correlate well ($R^2 = 0.82$, $P < 0.01$). The ET gaps in the year were filled using this relationship; the annual ET was then obtained by summing daily ET in the Taihu watershed.

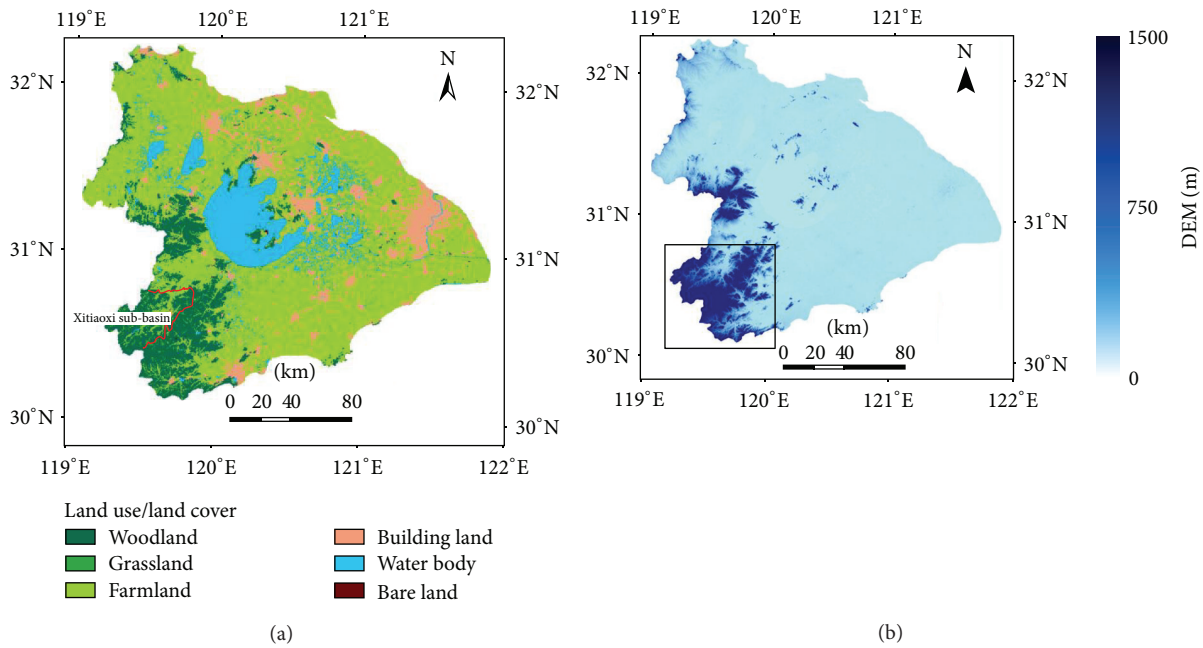

Figure 1: (a) Land cover map (a) and (b) digital elevation model (DEM) of the Taihu Basin in which the study area (in black square) was selected in mountainous areas.

2.2. Topographic Correction. The ET can be determined using Φ, R_n, G, and Δ, all of which can be estimated independently using remotely sensed data in accordance with (1)–(5). Among the variables in these equations, shortwave radiation R_s, longwave radiation R_l, T_s and T_a change substantially with the terrain features. The variability in elevation, surface orientation (slope and aspect), and shadows cast by topographic features create strong local radiation gradients. In this study, R_s was corrected based on a topographic correction of the albedo, and R_l was corrected based on a topographic correction of the T_s and T_a. The evaporative fraction EF was corrected based on a topographic correction of the T_s because the terrain effects on NDVI can generally be ignored [30]. Considering the effect of elevation on T_a, T_a was corrected using the DEM and the lapse rate (0.0065°C/m), which indicates that the air temperature decreases 0.65°C with a 100 m elevation increase. Terrain affects the satellite-retrieved T_s and ε_s values [31]. For the MODIS land surface temperature (T_s) product, only primary terrain information is considered in the bidirectional reflectance distribution function (BRDF) [32]; it ignores the terrain angular effect on T_s retrieval. Consequently, the angular effects on the combined T_s and ε_s were accounted for in the T_s terrain correction, which may be corrected using the following equation [31]:

$$T_s' = \left(\frac{T_s^4}{\cos\theta}\right)^{1/4}, \tag{6}$$

where T_s' is the corrected land surface temperature and θ is the angle between the satellite view path and is normal to the terrain element. The emitted radiance angle can be geometrically determined using the following equation:

$$\cos\theta = \cos\alpha\cos\beta + \sin\alpha\sin\beta\cos(\varphi_s - \varphi), \tag{7}$$

where α is the local slope angle, β is the sensor zenith angle, φ_s is the sensor azimuth angle, and φ is the aspect angle of the terrain element.

The terrain-induced angular effect on ρ can be corrected based on the cosine method as follows [33]:

$$\rho' = \frac{\rho}{\cos\theta}, \tag{8}$$

where ρ' denotes the corrected surface albedo.

In this study, we used (6) and (8) to correct the terrain effects on the key variables that is relevant to estimating the ET.

3. Study Materials and Data Processing

3.1. Study Area. The Taihu Basin in China was used as a case study due to its topographic features and data availability (Figure 1(a)). Lake Taihu is in the area bordered by the Yangtze River, Hangzhou Bay, and Qiantang River. The Taihu Basin covers 36500 km^2 and extends from 119.1°E to 122.2°E longitude and 30.0°N to 32.1°N latitude. It is a heterogeneous area characterized by mixed farming, forest, and grass lands. The area surrounding Lake Taihu is dominated by a monsoon climate. The annual average air temperature is 14.9–16.2°C, and the annual precipitation is between 1000 and 1400 mm. Farmland is the dominant land cover type in the Taihu Basin, which accounts for 59.8% of the total basin area; woodland area accounts for 13.4%, building land area accounts for

13.5%, water body area accounts for 13.0%, and grassland area accounts for 0.3% of the total basin area.

Figure 1(b) shows a digital elevation model (DEM) of the Taihu Basin. More than 80% of the area in the basin is flat with a 40 m average elevation. The mountainous area is located in the western and southwestern parts of the region, where the highest elevation is over 1500 m. A mountainous area in the southwest Taihu Basin was selected to illustrate the effects of topography (Figure 1(b)). The selected area, which is part of the Tianmu Mountains, extends from 30.0° to 31.0°N latitude and 119.5° to 120.5°E longitude and covers most of the mountainous areas in the Taihu Basin. The zonal vegetation is distributed vertically and includes evergreen broad-leaved and artificial bamboo forests below a 700 m elevation, mixed evergreen and deciduous forests at elevations between 850 and 1100 m, deciduous forests below a 1380 m elevation, and deciduous dwarf forest over a 1380 m elevation. Coniferous forests are spread sporadically at elevations between 300 and 1100 m.

To validate ET estimates using remote sensing, ET was estimated as a residual variable based on the principle of water balance in the subbasin. The Xitiaoxi subbasin, which is a closed subbasin upstream of the Taihu watershed, was used to validate the retrieved ET. The total monthly rainfall data from 10 rain gauge stations were collected. Monthly runoff data from the Fanjiacun hydrological station were obtained, which represent the total surface runoff in the Xitiaoxi subbasin. The data were provided by the Hydrological Bureau of Zhejiang Province.

3.2. Data Processing. The standard MODIS products from the Terra (EOS AM-1) satellites were used to estimate the regional ET. To avoid a cloud effect, we used a clear day on September 26 in 2006 (DOY 269) to examine the topographic effects on the ET estimates. This date included the growing season for the cropland and forest ecosystems, wherein the NDVI formed a gradient in the basin, which is implicitly required by the triangle method. The sensor zenith ranged from 0.5° to 13.8° with a 4.7° average on September 26, 2006, over the Taihu Basin, which implies that the remote-sensing image was screen under the point of vertical satellite direction, and the geometric image distortion was minimal this day.

The MODIS products were acquired from the Land Processes Distributed Active Archive Center (LP DAAC) (https://lpdaac.usgs.gov/). The selected products included MODIS geolocation (MOD03), the atmospheric profile product (MOD07), the surface reflectance (MOD09) and land surface temperature/emissivity product (MOD11_L2), all of which were generated using the Product Generation Executive (PGE) code Version 5. MOD03 contains the solar zenith and azimuth angles as well as satellite zenith and azimuth angles. MOD07 includes the air and dew point temperatures. MOD09 provides the surface reflectance through seven reflective bands and the values corrected for radiometric and atmospheric effects. MOD11_L2 provides the land surface temperature and surface emissivity in bands 31 and 32.

The NDVI values were retrieved from the surface reflectance in the red and near infrared (NIR) bands (MOD09). The 500 m data in the NIR band was resized to 250 m using a nearest-neighbor algorithm and again resized using the 250 m data in the red band to generate the 250 m NDVI. Likewise, the 1 km LST and 5 km T_a products were resized to a 250 m resolution using a nearest-neighbor algorithm. To estimate the pixel-by-pixel ET and EF, both the dry and wet edges in the $(T_s - T_a)$-NDVI space must be determined. For a given NDVI, the surface-air temperature difference $(T_s - T_a)$ increases gradually due to water stress in the surface soil from a minimum value $(T_{i,\min})$ at the wet edge to a maximum value $(T_{i,\max})$ at the dry edge, whereas the EF correspondingly decreases from a maximum to minimum value. In general, the wet edge is identified with the lowest $(T_s - T_a)$. In the Taihu Basin, the $T_{i,\min}$ remained stably within 0.5 K in DOY 269, 2006. The dry edge was determined using an automatically iterative method proposed by Tang et al. [25]. The linear relationship was determined as $T_{i,\max} = -5.5\text{NDVI} + 10.5$. The Φ values were subsequently derived from the dry and wet edges using an interpolation scheme (3) [10].

The surface net radiation (R_n) was estimated using (4b). The downward shortwave radiation was calculated using (A.2). The surface albedo was produced from surface reflectance in seven reflective bands using the narrowband-to-broadband conversion approach proposed by Liang [34]. The air emissivity was estimated from the air and dew point temperature data using (A.5) [35]. The broadband emissivity was generated from the narrowband emissivities in bands 31 and 32 [34]. In addition, the soil heat flux (G) was estimated from the NDVI using (5). For data processing, the parameters used to estimate R_n and G were resampled at a 250 m resolution before they were used in the estimation.

The 90 m Shuttle Radar Topography Mission (SRTM) data was used to generate the 250 m DEM data using the cubic convolution algorithm [36]. The 250 m DEM was used to generate the local slope and aspect angles of the terrain area. Equation (6) was used to correct the T_s data, and (8) was applied to correct ρ. The corrected values were used to derive R_n, EF, and, subsequently, ET. The R_n, EF, and ET values were also generated using uncorrected values. The ET values with and without the terrain correction were then compared to examine the topographic effects. The R_n and EF values with and without the terrain correction were also compared to investigate the major sources of the topographic effects on ET. Finally, the average values of the parameters before and after a topographic correction were calculated for the 8 slope classes in the terrain area. The relative error (RE) was used to evaluate the topographic influence in this study. The relative error can be expressed as follows:

$$\text{RE} = \frac{(V_{\text{after}} - V_{\text{before}})}{V_{\text{before}}} \times 100, \tag{9}$$

where V_{before} and V_{after} are the mean values of the parameters before and after the topographic correction, including the net radiation, evaporative fraction and ET.

4. Results and Discussion

The actual daily ET on DOY 269, 2006, for the Taihu Basin was derived using the triangle method with a topographic correction. The spatial variation for the estimated ET is shown. The effect of topography on ET and the contributing factors is analyzed.

4.1. Validation. Based on the principle of water balance, precipitation (P) in the watershed equals the sum of the ET and runoff (P = ET+Runoff) when the variation in watershed soil water content on an annual scale is ignored. Therefore, we can compare the sum of the estimated subwatershed ET and runoff with precipitation and validate watershed ET in the Xitiaoxi subwatershed. Based on meteorological and hydrological station, the observed annual total precipitation in 2006 was 1214.12 mm; the corresponding observed annual runoff depth was 514.89 mm. The estimated annual ET by remote sensing data was 825.09 mm before topographic correction and 649.30 mm after topographic correction in the subwatershed. Based on the principle of water balance, the water budget difference ($\Delta D = P - \text{Runoff} - \text{ET}$) is the error for the ET retrieved from remote sensing if the observed precipitation and runoff data are highly accurate. The ΔD in 2006 was 125.86 mm and −49.93 mm before and after topographic correction, respectively. The average relative error of the retrieved ET was 18.0% and −7.1% before and after topographic correction, respectively, compared with ground-based water components in 2006. The validation results indicate that the ET retrieved using the triangle method before the topographic correction was overestimated by 18.0%, while the relative error of the retrieved ET after the correction was reduced by 7.1%, which demonstrates remarkably improved accuracy in the estimated ET.

Notably, direct validation of topographic effect is yet unavailable and the present validation with the water balance approach is applicable at an annual scale. The annual ET estimation may be influenced by the temporal upscaling strategy and the triangle method, in addition to topographic effect. Given the same upscaling strategy and ET estimation approach, the annual difference between the estimated ET values with and without the correction was attributable to topographic effect.

4.2. Topographic Features of the Selected Mountainous Area. The selected mountainous area accounts for 9% of the Taihu Basin (Figure 1(b)). The aspect angle, elevation, and slope in the selected area range from 0.11° to 360°, 5 m to 1509 m (244 m on average) and 0° to 69.29° (7.88° on average), respectively. Most of the area (over 84%) is located below a 400 m elevation, and less than 1% of area is higher than 1200 m (Figure 2(a)). More than 73% of the area has a slope less than 20° (Figure 2(b)). The frequency distribution of the aspect angle is similar across eight different direction bins and averages 12% (Figure 2(c)); it was greater from 45° to 180° than 180° to 315°. The relationship between elevation and slope (Figure 2(d)) indicates that the slope increases with elevation below 800 m and then decreases with elevation until approximately 1200 m. The mean slope is greater than 20° above a 1200 m elevation, which includes less than 0.1% of the selected area. Based on these statistics, the selected area includes a wide range of elevations and slopes with a nearly constant aspect angle distribution for the topographic analyses.

4.3. Effects of Topographic Correction on the ET. The ET spatial distribution over the Taihu Basin is shown in Figure 3. Lake Taihu and other water bodies exhibited the highest ET values, averaging 6.5 mm day^{-1}. Elsewhere, the ET values range from 4.5 mm day^{-1} to 6 mm day^{-1} in flat regions in the north and southeast due to the farmland and grassland distribution. Before topographic correction, most of the ET values over the mountainous areas were, on average, lower than the values over flat regions, except for high values (more than 6 mm day^{-1}) in the southwestern Taihu Basin area (Figure 3(a)). This observation indicates that the ET estimated using the triangle method may include a large bias over mountainous areas. After the topographic correction, the ET values over the mountainous areas were much lower than that before the topographic correction (Figure 3(b)). Furthermore, the ET values before correction showed an increasing trend with elevation, and the maximum ET values reached 6-7 mm day^{-1} in the selected region (Figure 3(c)). In contrast, the ET values reduced to 3 mm day^{-1} on average after the topographic correction (Figure 3(d)). Moreover, there were obviously differences in ET distribution for different aspect angles of the terrain. The ET values for the south-facing slopes were lower than for the north-facing slopes, and this was alleviated after the correction.

The net radiation and evaporative fraction were the key parameters used to estimate the regional ET. The R_n and EF between the data before and after the topographic correction were compared over the selected region (shown in Figure 4). The R_n before correction ranged from 200 to 400 Wm^{-2}, the high R_n value was generated for the south and southwest areas (Figure 4(a)); however, a slight decrease was observed after the topographic correction, especially in the high-altitude mountainous areas (Figure 4(b)). For the EF, a distinct decease was observed in the mountainous area after the correction (Figures 4(c) and 4(d)); the pattern clearly differed between the north- and south-facing slopes. Previous research shows that the cosine correct method for remote sensing images overcorrects when the slope is greater than 30° [37]. However, the overcorrection phenomenon only slightly influences the selected region because the area dominated by a high slope (>30°) was <1%.

A comparison of the daily ET values before and after the topographic correction over the selected region is shown in Table 1. The corrected daily ET decreased by 7.0%–37.3% for different aspect angles. The relative error for the aspect angles between 180° and 360° (19.5%–37.3%) was greater than for the aspect angles between 0 and 180° (7.0%–12.7%); the largest error was observed for aspect angles between 225° and 315°.

Figure 5 shows the ET response to elevation and slope at different aspect angles over the selected area in the Taihu Basin. The daily ET before correction distinctly increased

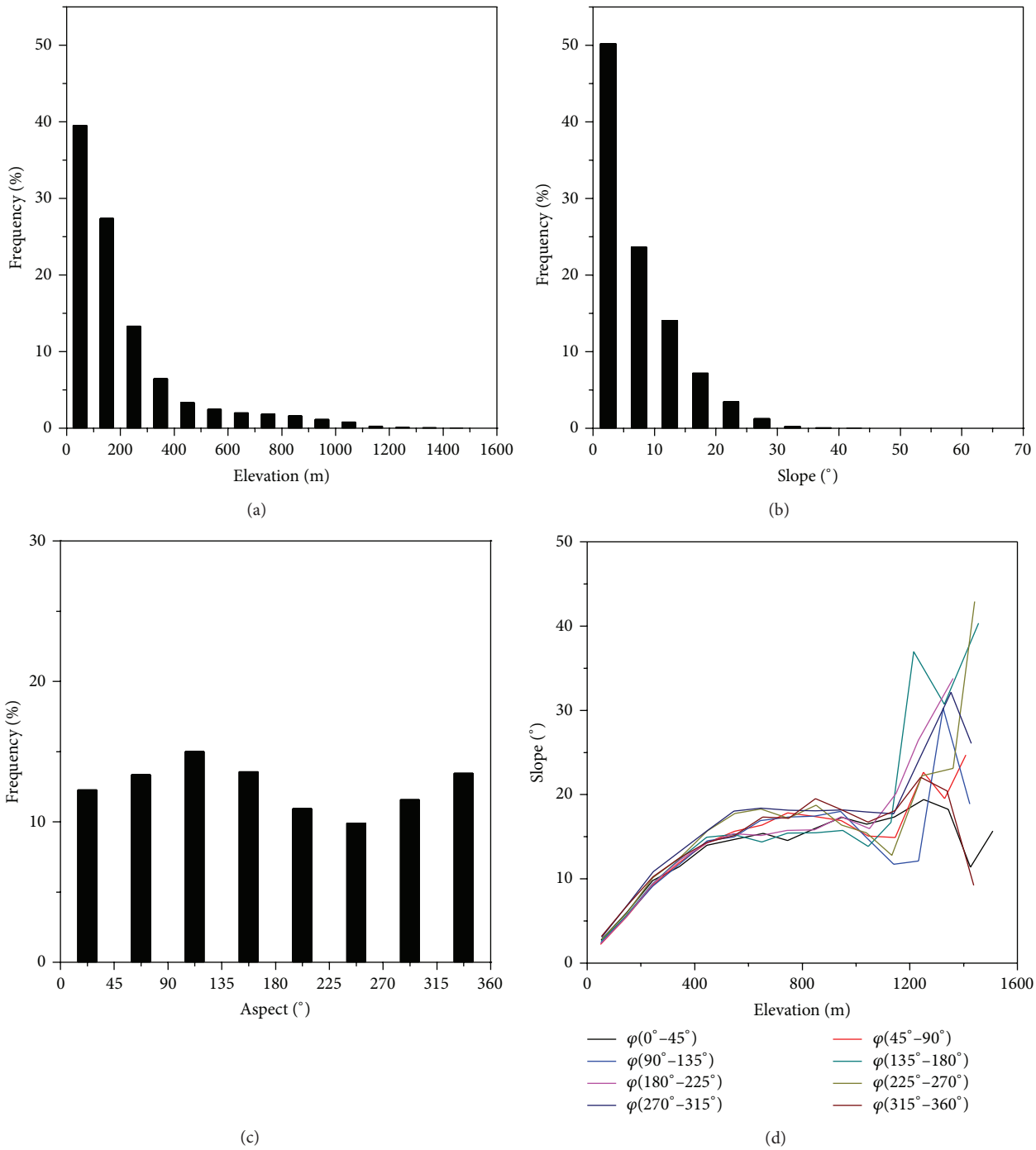

Figure 2: Frequency distributions of the (a) elevation, (b) slope, (c) aspect angle of terrain and (d) relationship between the elevation and slope over the selected Taihu Basin area.

with elevation and slope (Figures 5(a) and 5(c)). The ET was lower after the correction than before. After the correction, the ET slightly increased with elevation, ranging from 4.1 mm day^{-1} to 8.0 mm day^{-1} for aspect angles from 0 to 180° (north facing) (Figure 5(b)), while for other aspect angles, the ET tended to decrease below a 800 m elevation and increase over 800 m, ranging from 0.5 mm day^{-1} to 4.6 mm day^{-1}. Furthermore, the ET magnitude and range varied with the aspect angle. Figure 5(d) shows that the corrected ET dramatically decreased with the slope, especially for aspect angles from 180° to 360°. ET decreased by 90% from 6.8 mm day^{-1} to 0.6 mm day^{-1} at slopes over 50°. The lower ET values were observed for south-facing slopes, which may be due to a soil moisture deficiency and net radiation [28]. The topographic effect is vegetation dependent [38, 39]. Gao et al. [28] indicated different responses of ET estimates to elevation

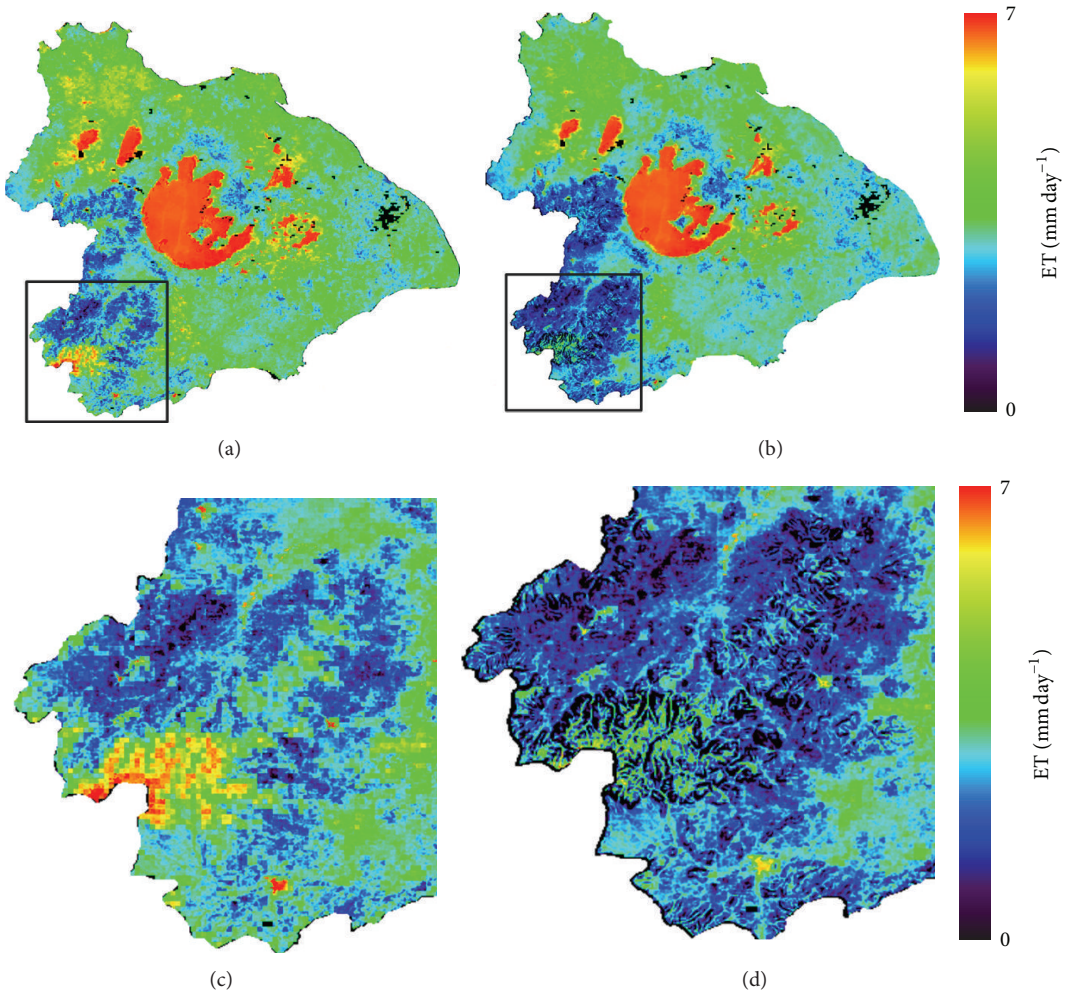

Figure 3: The evapotranspiration map over the Taihu Basin for September 26, 2006, (a) before the topographic correction and (b) after the topographic correction. The area in the black square is the selected mountainous area. Zoom in on the selected area for the (c) ET before the topographic correction and (d) ET after the topographic correction. Except for the low values in the selected area, the black scatter indicates missing data.

in south-facing woodland and grassland. The grassland ET estimate was lower than in the woodland at elevations ranging from 1200 m to 1600 m, mainly due to the lower average LAI in the grassland. The low ET values at elevations ranging from 600 m to 800 m could be attributed to the coniferous forest distribution in the selected region.

4.4. Environmental Influence on ET Estimates. Based on (1), the regional ET was estimated using the R_n, G, and EF. The R_n was estimated using (4a) and (4b). Among the variables in the equations, the surface temperature (T_s) and albedo were sensitive to topographic angular effects. The T_s and albedo increased by 0.22%–1.01% and 0.79%–4.35%, respectively, after the topographic correction (Table 2). The relative errors of the two parameters for the aspect angles 180° to 360° were also greater than for the other aspect angles; these observations differ from the results in Wen et al. [40], where the corrected forest albedo increased in north-facing pixels and decreased in south-facing pixels. The T_s and albedo increases induced increases in the upward longwave and shortwave radiation, which induced a decrease in the daily

Table 1: A comparison of the daily ET before and after the topographic correction for different terrain aspect angles over the selected area.

Topographic correction	Daily ET (mm day^{-1})		Relative error (RE)
	Before	After	
φ (0–45°)	5.51	4.81	−12.7%
φ (45°–90°)	5.7	5.12	−10.2%
φ (90°–135°)	5.48	5.10	−7.0%
φ (135°–180°)	5.21	4.60	−11.8%
φ (180°–225°)	5.11	4.12	−19.5%
φ (225°–270°)	5.30	3.32	−37.3%
φ (270°–315°)	5.39	3.01	−44.2%
φ (315°–360°)	5.39	3.91	−27.5%

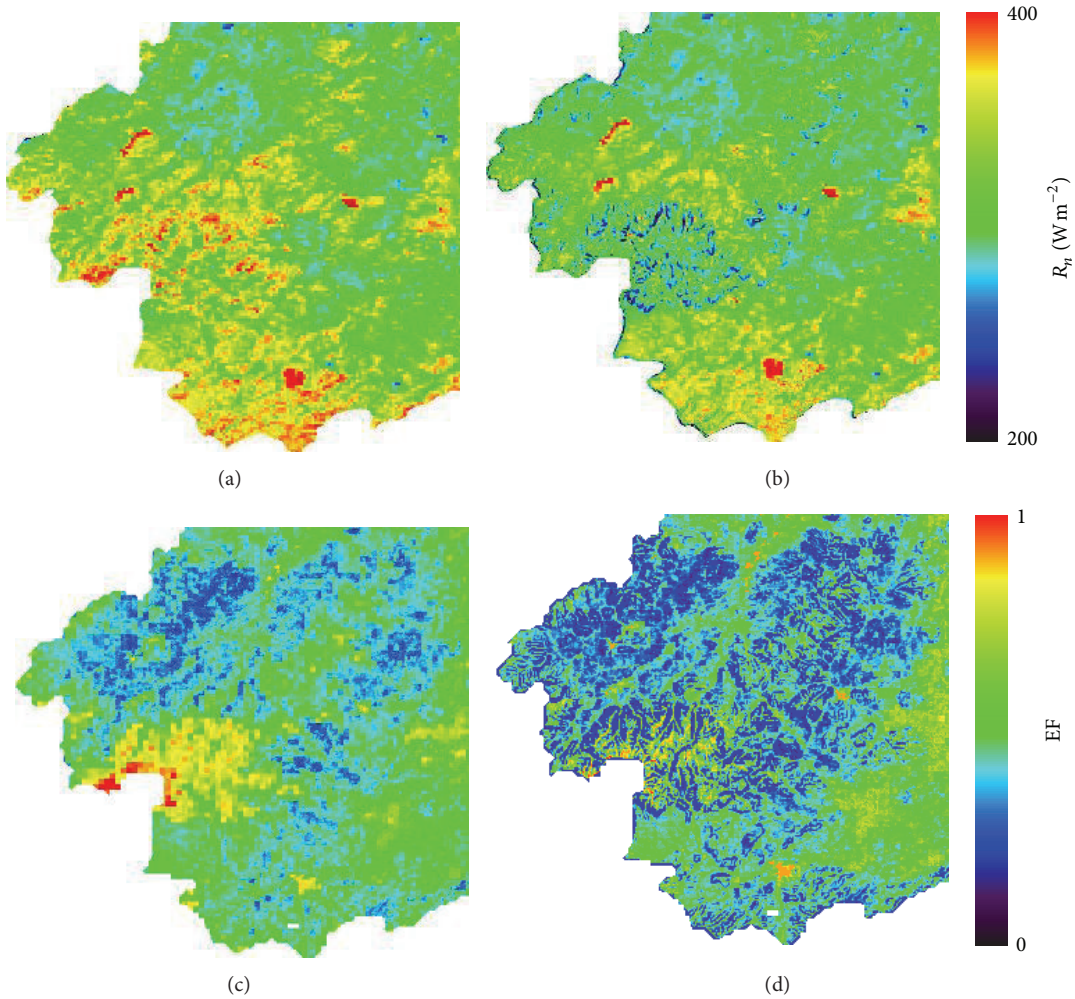

Figure 4: A map of net radiation (R_n) and evaporative fraction (EF) on September 26, 2006, over the selected Taihu Basin region; (a) the R_n before topographic correction, (b) R_n after topographic correction, (c) EF before topographic correction, and (d) EF after topographic correction.

R_n. Thus, after the topographic correction, the R_n decreased by 0.63%–3.17%, and the G decreased by 0.78%–2.99% (Table 2).

The EF was estimated using (2) and (3); the EF is relevant to the NDVI and T_s. Based on Table 2, the NDVI is not distinctly different for the four terrain aspect angles with a 0.73 average. The corrected EF decreased by 9.3%–48.8% for the different aspect angles. Of the parameters in Table 2, the largest relative error was observed for the aspect angles 225°–315° because the sensor azimuth angle ranged from 90° to 105°, which yielded the lowest $\cos\gamma$ in (7) among the aspect angles.

The large correction in the EF was mainly attributed to the T_s correction; however, the T_s correction varied over a small range. To explain this phenomenon, the (T_s – T_a)-NDVI triangle space was analyzed (Figure 6). The two boundaries of the LST/NDVI feature space are limiting conditions for the surface fluxes. The dry edge represents the minimum ET with unavailable of soil moisture for different vegetation index. The wet edge that corresponds to lower temperatures represents the potential ET with unlimited soil water availability for different vegetation indices. An implicit assumption of the triangle method is that the ET primarily depends on soil moisture and vegetation cover. This assumption requires a heterogeneous area with a full range of possible soil moisture and vegetation index values as well as simultaneous relatively uniform atmospheric forcing [41].

The triangle approach requires a full range of soil moisture and vegetation index for reliable determination of the dry and wet edges in study area. This is usually hard to satisfy for a relatively small area, for example, the selected mountainous area. Instead, the whole basin was used to determine the edges to satisfy the underlying assumption (Figures 6(a) and 6(b)). Furthermore, the dry and wet edges were determined for the case with topographic correction, and were applied to the case without correction. The reasons are (1) the MODIS T_s and T_a product was only corrected for the selected region, which only slightly influences the (T_s – T_a)-NDVI triangle space in the entire Taihu Basin; (2) the EF was controlled by the relationship between the (T_s – T_a) and NDVI (the dry and

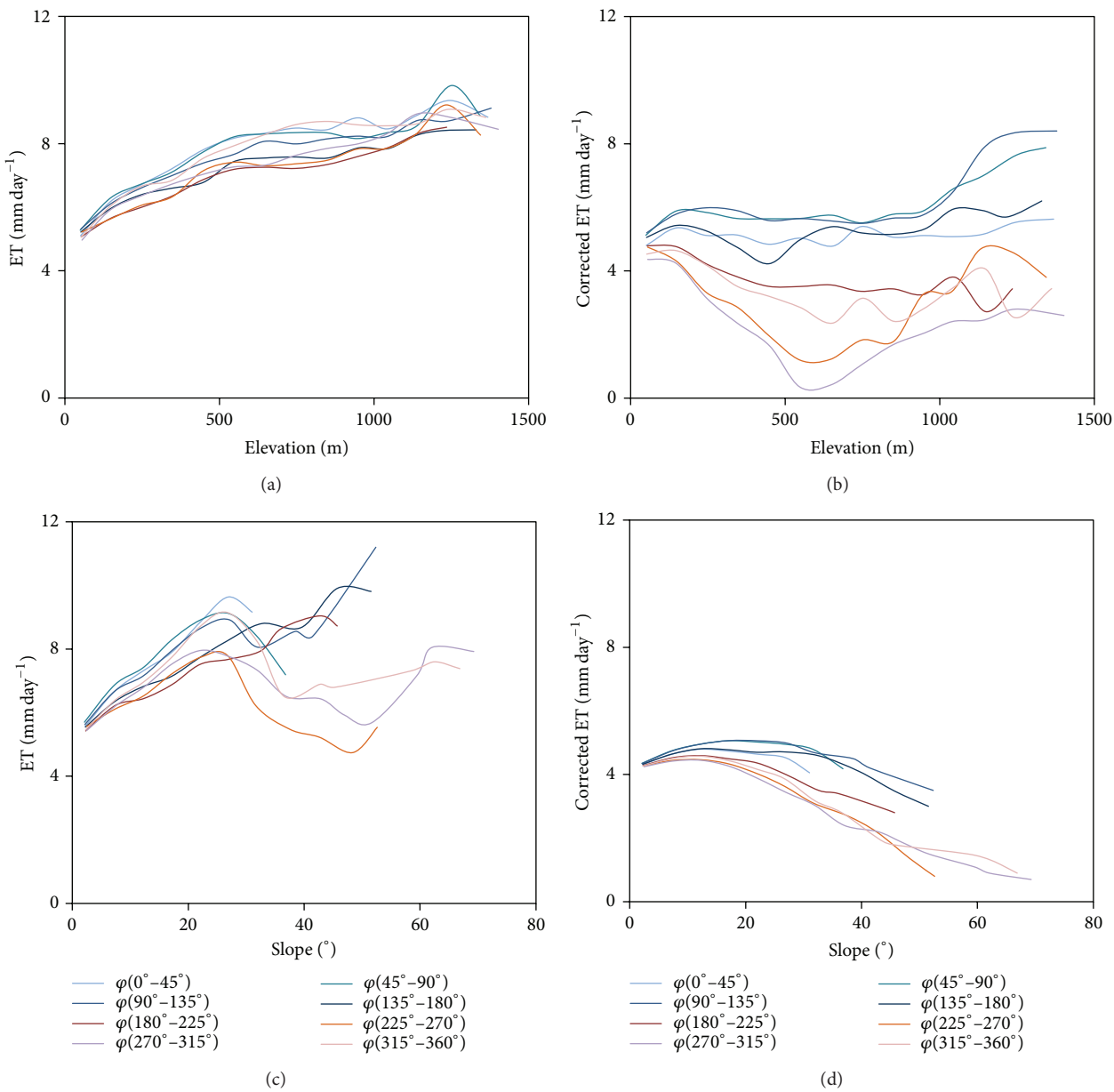

Figure 5: The ET response to elevations and slopes for different aspect angles of terrain (φ) over the selected Taihu Basin area. (a) The elevation before the topographic correction, (b) elevation after the topographic correction, (c) slope before the topographic correction, and (d) slope after the topographic correction.

wet edges). When the edges were stable, the EF changes were only generated by the corrected ($T_s - T_a$); thus, the relative influence of the topographic correction on the ET estimate can be evaluated. The ($T_s - T_a$)-NDVI spatial distribution in the selected area (Figures 6(c) and 6(d)) composed part of the region, so the dry and wet edges in the entire Taihu Basin were used in the selected area (Figures 6(a) and 6(b)).

MODIS T_s products are typically underestimated over mountain areas [42]. Figure 6(c) shows that the ($T_s - T_a$) before correction is lower than the wet edge when the NDVI is near 0.8, which produced an overestimated EF. However, the corrected T_s values increased with the corresponding NDVI values. Most corrected (T_s–T_a) values were distributed between the dry and wet boundaries (Figure 6(d)). The abnormal phenomenon in Figure 6(d) shows that a high ($T_s - T_a$) value correlated with a high NDVI; the ($T_s - T_a$)-NDVI space seemed inverse to the variation trend in the selected region. However, the local spatial distribution cannot represent the ($T_s - T_a$)-NDVI relationship throughout the entire region. The relationship between ($T_s - T_a$) and NDVI was controlled by the soil moisture conditions [4]. In the selected region, the available soil moisture decreased with a rising elevation and slope, which corresponds to a lower ET and higher surface temperature for different vegetation

Table 2: The mean value and relative error (RE) of the surface parameters and energy fluxes before and after the topographic correction for the different terrain aspect angles over the selected area.

	Correct	φ (0–45°)	φ (45°–90°)	φ (90°–135°)	φ (135°–180°)	φ (180°–225°)	φ (225°–270°)	φ (270°–315°)	φ (315°–360°)
NDVI		0.74	0.73	0.72	0.71	0.72	0.72	0.73	0.73
T_s (K)	Before	299.28	299.06	299.27	299.55	299.65	299.46	299.40	299.44
	After	300.44	299.89	299.92	300.42	301.16	301.96	302.41	301.44
	RE (%)	0.39	0.28	0.22	0.29	0.50	0.83	1.01	0.67
Albedo	Before	0.118	0.122	0.126	0.127	0.127	0.122	0.115	0.115
	After	0.120	0.124	0.127	0.129	0.129	0.127	0.120	0.118
	RE (%)	1.69	1.64	0.79	1.57	1.57	4.10	4.35	2.61
Daily R_n (W m^{-2})	Before	370.37	368.48	367.14	366.38	366.02	367.13	370.23	370.99
	After	366.03	365.35	364.63	363.00	360.16	357.45	358.50	363.32
	RE (%)	−1.17	−0.85	−0.68	−0.92	−1.60	−2.64	−3.17	−2.07
Daily G (W m^{-2})	Before	46.98	47.4	47.93	49.60	48.93	48.99	48.43	47.75
	After	46.48	47.03	47.63	49.20	48.20	47.79	46.98	46.79
	RE (%)	−1.06	−0.78	−0.63	−0.81	−1.49	−2.45	−2.99	−2.01
EF	Before	0.43	0.44	0.43	0.42	0.41	0.42	0.43	0.42
	After	0.35	0.39	0.39	0.36	0.31	0.25	0.22	0.28
	RE (%)	−18.6	−11.4	−9.3	−14.3	−24.4	−40.5	−48.8	−33.3

indices. The scatters of lower ET should be close to the dry edge in the $(T_s - T_a)$-NDVI space.

Based on (3), the EF estimate depended on the normalized difference temperature index $(T_{i,\max} - T_i)/(T_{i,\max} - T_{i,\min})$. Using the dry and wet boundaries in the $(T_s - T_a)$-NDVI triangle space (Figure 6), $(T_{i,\max} - T_{i,\min})$ decreased with an increasing NDVI. In the topographic area with high NDVI values, the $(T_s - T_a)$ values were small compared with the absolute $(T_s - T_a)$ values but large compared with $(T_{i,\max} - T_{i,\min})$, which can cause large variations in the EF correction. In the selected area, the $(T_i' - T_i)/(T_{i,\max} - T_{i,\min})$ ranged from 6.5% to 29.3% for different aspect angles (averaging 8.7% for the aspect angles 0°–180° and 21.3% for the aspect angles 180°–360°). The ET topographic correction was similar to the EF and is attributed to the T_s correction. Thus, the T_s topographic correction was more important to the ET estimate over a complex terrain, especially using the triangle method.

4.5. Influence of Topographic Parameters. The R_n and EF responses to elevation and slope for different aspect angles over the selected Taihu Basin area are shown in Figures 7 and 8. The corrected R_n decreased with increased elevation (Figure 7(b)), which is the opposite of estimates before the correction was applied (Figure 7(a)). Moreover, the degree to which R_n decreased for aspect angles from 180° to 360° was greater than for other aspect angles. The mean R_n varied with elevation from 328 W m^{-2} to 372 W m^{-2} after the correction was applied. The varying trend for net radiation with elevation was determined using the combined effects of net shortwave and longwave radiation. On one hand, the air density and water content in the atmosphere tend to decrease with increased elevation, which produces an increase in atmospheric transmissivity and direct solar radiation. However, diffuse solar radiation decreases with an elevation increase, thus limiting the increase in total shortwave radiation [43]. On the other hand, the air temperature at the screen level and T_s decrease with increased elevation, which simultaneously reduces atmospheric downwelling and surface upwelling longwave radiation [43]. Eventually, the net radiation decreased slightly with increased elevation. The EF response to elevation was similar to ET. The EF values for the south-facing slopes were lower than for the north-facing slopes; the mean EF varied with elevation from 0.05 to 0.8 after the correction.

Figure 8 shows that, after the correction, both the R_n and EF dramatically decreased with the slope, especially for aspect angles from 180° to 360°. The corrected R_n decreased by 40% from an average of 358 W m^{-2} to 225 W m^{-2} for slopes greater than 50°. The corrected EF decreased with the slope instead of increasing, which characterized the estimate before the correction. Based on Figures 8 and 2(d), most areas with large slopes (15° on average) range in elevation from 600 m to 800 m, which indicates that the low EF and ET values between the elevations at 600 and 800 m are mainly due to the large terrain slopes. The south-facing slope surfaces receive more sunlight, which heats the surface and may enhance turbulent mixing of air mass. More R_n energy was then partitioned into a sensible heat flux, which decreases the latent heat flux (ET). Gao et al. [28] also indicated that the corrected ET for south-facing woodland and grassland tended to decrease with increasing elevation.

Based on Figures 5, 7, and 8, the topographic parameters (elevation, slope, and aspect angle) strongly influence the ET, R_n, and EF estimates. Among these parameters, the aspect angles affect the ET magnitude and trend, especially for north-facing and south-facing slopes. The ET, R_n and EF variations were more sensitive to slope than to elevation.

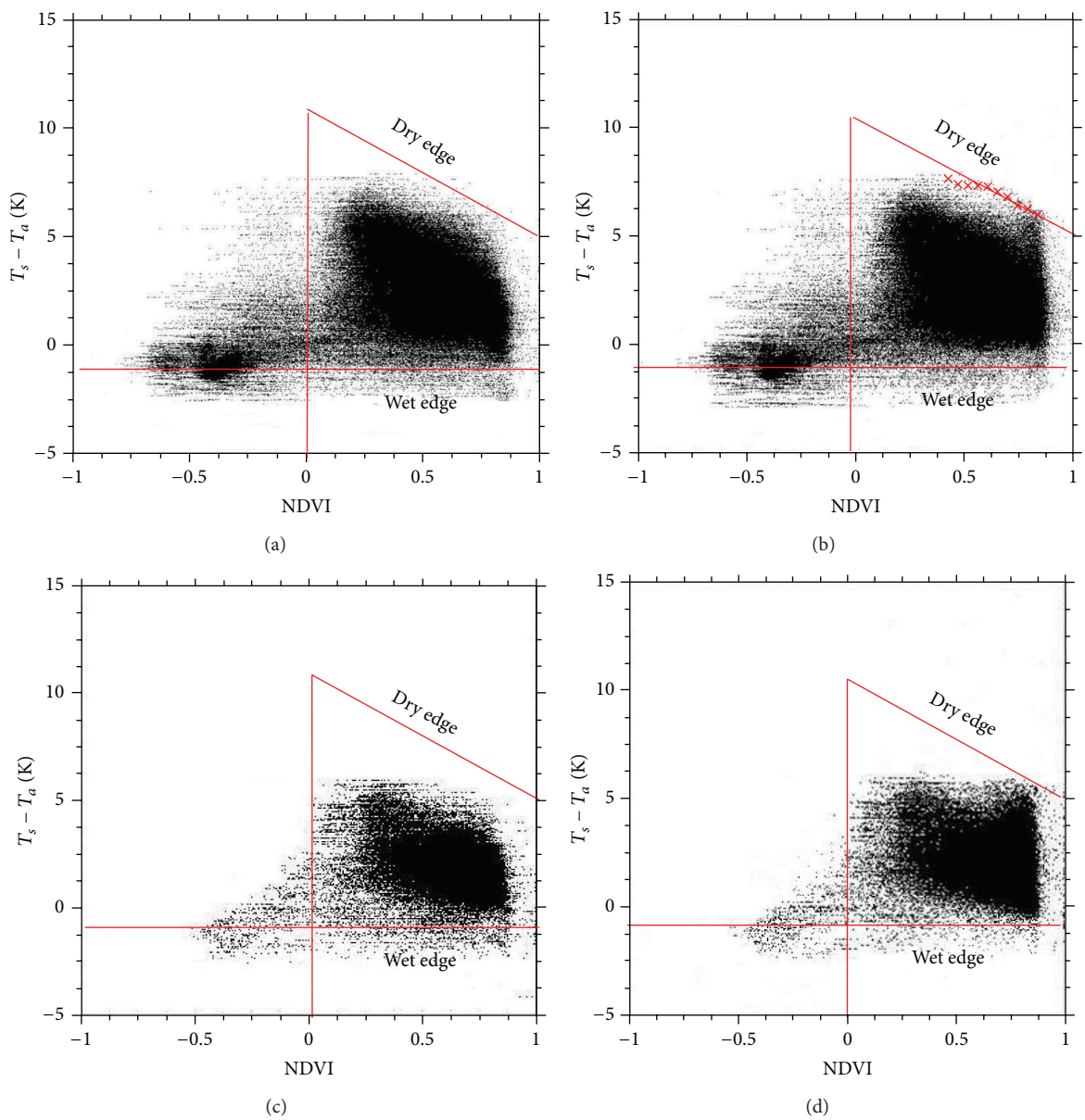

Figure 6: The surface-air temperature differences in the Normalized Difference Vegetation Index ($T_s - T_a$)-NDVI scatter plots for a clear-sky day (Sept. 26, 2006) from MODIS data over the Taihu Basin. (a) Before the topographic correction, (b) after the topographic correction, (c) before the topographic correction over the selected area, and (d) after the topographic correction over the selected area. The dry (upper red line) and wet (lower red line) edges represent the maximum ET and minimum ET, respectively. The cross points of red lines, estimated by an automatically iterative method [25], were used to determine dry edges.

In this study, the cosine correction method was applied to ET estimates through topographic correction on the net radiation and evaporative fraction. This correction method for net radiation does not involve a complex radiative transfer model. Nevertheless, the cosine method does not consider diffuse irradiance from atmospheric and terrain sources, and it has an overcorrection problem [44, 45]. Assuredly, an improvement in the (T_s – T_a)-NDVI triangular space will significantly improve the ET estimate accuracy, particularly its spatial distribution across large heterogeneous areas.

We should emphasize that our purpose was to evaluate the relative contribution of the topographic influence using the triangle approach to evapotranspiration estimates over mountainous areas. The ET estimates after the topographic correction was more reasonable than before the topographic correction; in particular, they exhibited realistic spatial variability across mountainous areas. In addition, the results for the influence of terrain on ET variations showed similar findings as in other studies [28, 43, 44, 46].

5. Conclusion

Remote sensing provides land surface characteristics at fine temporal and regional spatial scales to retrieve parameters

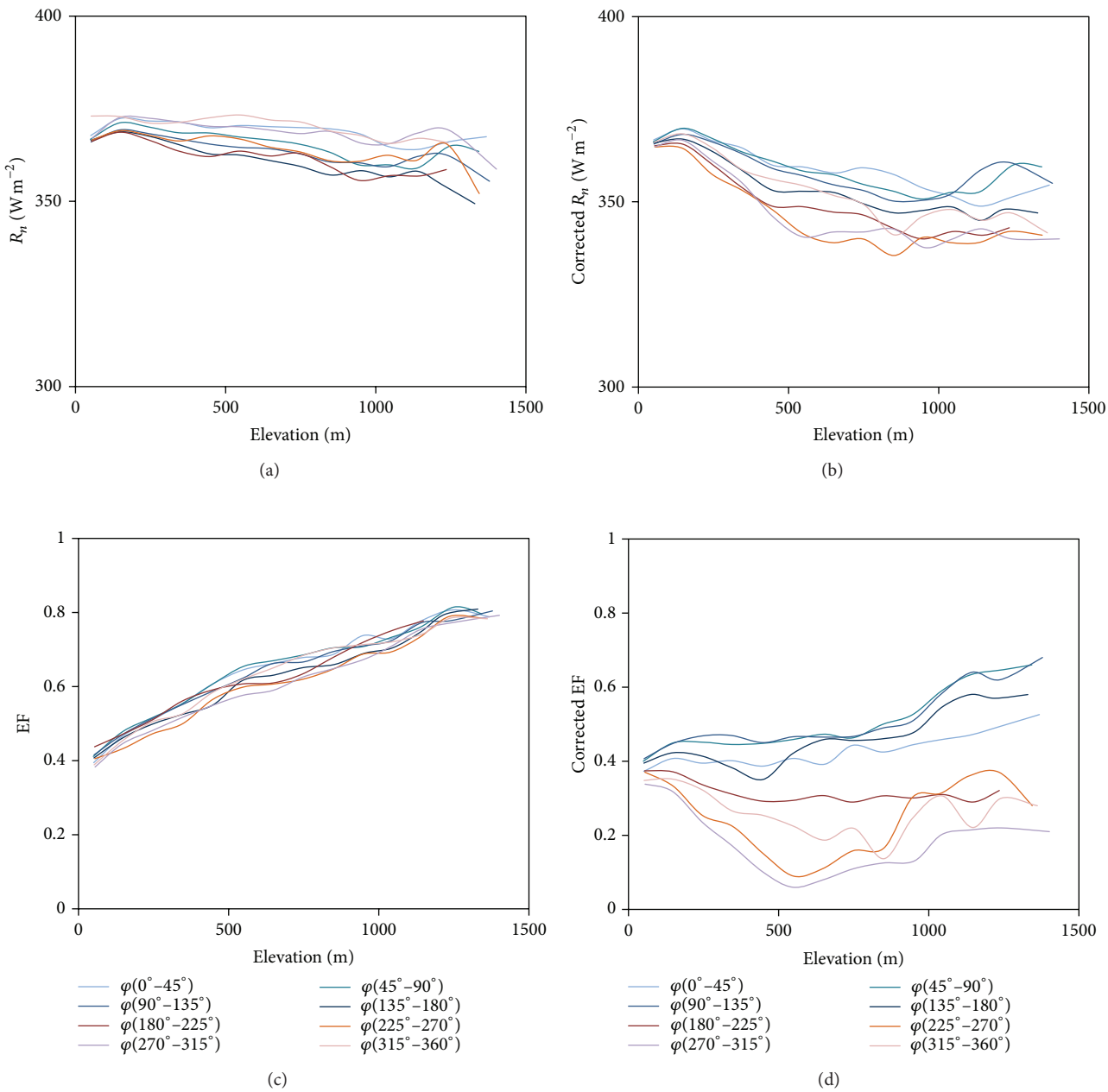

Figure 7: The relationship between R_n, EF, and elevation for different terrain aspect angles (φ) over the selected Taihu Basin area. (a) The R_n before the topographic correction, (b) R_n after the topographic correction, (c) EF before the topographic correction, and (d) EF after the topographic correction.

relevant to land processes. Evapotranspiration cannot be measured directly from satellite observations, but it can be estimated by retrieving the evaporative fraction and net radiation from remote sensing data. The evaporative fraction was obtained from MODIS data using the triangle method. The net radiation was also retrieved from MODIS data. Considering the terrain and satellite angles, we performed topographic corrections for the triangle method to estimate the regional ET. The topographic parameters strongly influence ET. The corrected daily ET values decreased with elevation and slope; the relationships were more sensitive to slope than elevation. Furthermore, the ET magnitude and range varied with the aspect angle. The corrected ET decreased by an average of 10.4% and 32.1% for north- and south-facing slopes, respectively, over the selected Taihu Basin area. The topographic correction for ET was consistent with the EF correction, which strongly depends on the surface temperature correction. Although the topographic corrections were performed to evaluate ET retrieval over a complex terrain area, more carefully designed examinations or experiments are necessary to more comprehensively understand the relevant issues.

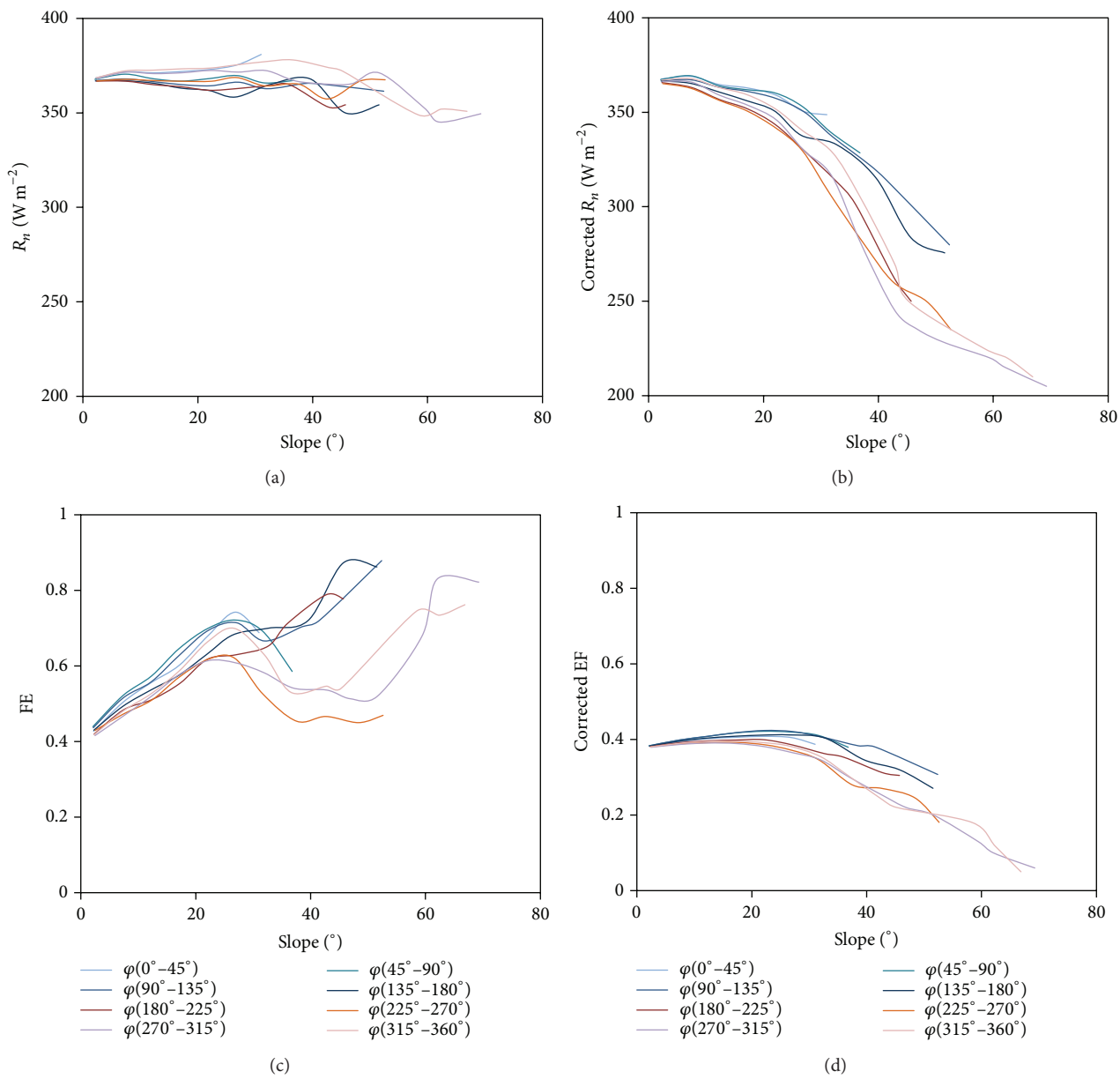

Figure 8: The relationship between R_n, EF, and slope for different terrain aspect angles (φ) over the selected area of the Taihu Basin. (a) R_n before topographic correction, (b) R_n after topographic correction, (c) EF before topographic correction, and (d) EF after topographic correction.

Appendices

A. Estimation of Net Radiation Using MODIS Data

Based on (4a) and (4b), the instantaneous R_n includes four components of downward and upward shortwave radiation fluxes and downward and upward longwave radiation fluxes.

The downward shortwave radiation can be expressed as follows [47]:

$$R_s^{\downarrow} = S_0 \tau_{sw} \cos\theta, \tag{A.1}$$

where τ_{sw} is the atmospheric clear sky shortwave transmission factor, S_0 is the solar constant at the top of the atmosphere, which is approximately 1367 W m^{-2}, and θ is the solar zenith angle. For this study, we used the parameterization scheme developed by Zillman [48]:

$$R_s^{\downarrow} = \frac{S_0 \cos^2\theta}{d}, \tag{A.2}$$

where $d = 1.085\cos\theta + e_0\,(2.7 + \cos\theta) \times 10^{-3} + 0.1$ and e_0 is the water vapor pressure (hPa).

The longwave radiation can be expressed using the Steffan-Boltzmann equation:

$$R_L^{\downarrow} - R_L^{\uparrow} = \sigma\varepsilon_a T_a^4 - \sigma\varepsilon_s T_s^4, \quad (A.3)$$

where ε_a is the air emissivity, ε_s is the surface emissivity, T_a is the air temperature (K) at screen level, T_s is the land surface temperature (K), and $\sigma = 5.67 \times 10^{-8}\,\mathrm{W\,m^{-2}\,K^{-4}}$ is the Steffan-Boltzmann constant.

The ε_s value was calculated using the following nonlinear formula [34]:

$$\varepsilon_s = 0.273 + 1.778\varepsilon_{31} - 1.807\varepsilon_{31}\varepsilon_{32} - 1.037\varepsilon_{32} + 1.774\varepsilon_{32}^2, \quad (A.4)$$

where ε_{31} and ε_{32} denote the emissivity in bands 31 and 32, respectively. The ε_a value was estimated using the scheme given by Prata [35]:

$$\varepsilon_a = \left[1 - (1+\xi)\exp\left\{-(1.2+3\xi)^{1/2}\right\}\right], \quad (A.5)$$

where $\xi = 46.5e_0/T_a$. The water vapor pressure e_0 can be estimated using the dew point temperature according to the Clausius-Clapeyron equation:

$$e_0 = 6.11\exp\left[\frac{L_v}{R_v}\left(\frac{1}{T_0} - \frac{1}{T_d}\right)\right], \quad (A.6)$$

where L_v is the latent heat of vaporization ($2.5 \times 10^6\,\mathrm{J\,kg^{-1}}$), R_v is the gas constant for water vapor ($461\,\mathrm{J\,kg^{-1}\,K^{-1}}$), $T_0 = 273$ K, and T_d is the dew point temperature (K) at screen level.

B. Daily R_n Estimation

Bisht et al. [49] proposed a sinusoidal model to estimate the diurnal cycle of net radiation for clear sky days, which closely follows the framework of Lagouarde and Brunet's [50] model of the diurnal cycle of surface temperature. The sinusoidal model is given as follows:

$$R_n(t) = R_{n\_\max}\sin\left[\left(\frac{t - t_{\mathrm{rise}}}{t_{\mathrm{set}} - t_{\mathrm{rise}}}\right)\pi\right], \quad (B.1)$$

where $R_{n\_\max}$ is the maximum value of R_n estimated during the day and t_{rise} and t_{set} are the local times at which R_n becomes positive and negative, respectively. For a given study day, the satellite overpass time (overpass), sunrise time (t_{rise}), and sunset time (t_{set}) are known, so the value of $R_{n\_\max}$ can be obtained from the corresponding value of the INR estimate.

Conflict of Interests

The authors declare that there is no conflict of interests regarding the publication of this paper.

Acknowledgments

This work was jointly supported by a Key Program of Nanjing Institute of Geography and Limnology of the Chinese Academy of Sciences (NIGLAS2012135001) and the National Natural Science Foundation of China (no. 40901162). MODIS data were obtained from the website of http://ladsweb.nascom.nasa.gov/.

References

[1] B. J. J. M. van den Hurk, W. G. M. Bastiaanssen, H. Pelgrum, and E. van Meijgaard, "A new methodology for assimilation of initial soil moisture fields in weather prediction models using meteosat and NOAA data," *Journal of Applied Meteorology*, vol. 36, no. 9, pp. 1271–1283, 1997.

[2] W. G. M. Bastiaanssen, D. J. Molden, and I. W. Makin, "Remote sensing for irrigated agriculture: examples from research and possible applications," *Agricultural Water Management*, vol. 46, no. 2, pp. 137–155, 2000.

[3] Z. Su, "Remote sensing of land use and vegetation for mesoscale hydrological studies," *International Journal of Remote Sensing*, vol. 21, no. 2, pp. 213–233, 2000.

[4] T. Carlson, "An overview of the "triangle method" for estimating surface evapotranspiration and soil moisture from satellite imagery," *Sensors*, vol. 7, no. 8, pp. 1612–1629, 2007.

[5] N. Batra, S. Islam, V. Venturini, G. Bisht, and L. Jiang, "Estimation and comparison of evapotranspiration from MODIS and AVHRR sensors for clear sky days over the Southern Great Plains," *Remote Sensing of Environment*, vol. 103, no. 1, pp. 1–15, 2006.

[6] R. D. Jackson, R. J. Reginato, and S. B. Idso, "Wheat canopy temperature: a practical tool for evaluating water requirements," *Water Resources Research*, vol. 13, no. 3, pp. 651–656, 1977.

[7] J. L. Hatfield, "Evapotranspiration obtained from remote sensing methods," *Advances in Irrigation*, vol. 2, pp. 396–416, 1983.

[8] J. M. Norman, W. P. Kustas, and K. S. Humes, "Source approach for estimating soil and vegetation energy fluxes in observations of directional radiometric surface temperature," *Agricultural and Forest Meteorology*, vol. 77, no. 3-4, pp. 263–293, 1995.

[9] M. S. Moran, T. R. Clarke, Y. Inoue, and A. Vidal, "Estimating crop water deficit using the relation between surface-air temperature and spectral vegetation index," *Remote Sensing of Environment*, vol. 49, no. 3, pp. 246–263, 1994.

[10] L. Jiang and S. Islam, "A methodology for estimation of surface evapotranspiration over large areas using remote sensing observations," *Geophysical Research Letters*, vol. 26, no. 17, pp. 2773–2776, 1999.

[11] G. Boni, D. Entekhabi, and F. Castelli, "Land data assimilation with satellite measurements for the estimation of surface energy balance components and surface control on evaporation," *Water Resources Research*, vol. 37, no. 6, pp. 1713–1722, 2001.

[12] J. C. Price, "Using spatial context in satellite data to infer regional scale evapotranspiration," *IEEE Transactions on Geoscience and Remote Sensing*, vol. 28, no. 5, pp. 940–948, 1990.

[13] T. N. Carlson, R. R. Gillies, and T. J. Schmugge, "An interpretation of methodologies for indirect measurement of soil water content," *Agricultural and Forest Meteorology*, vol. 77, no. 3-4, pp. 191–205, 1995.

[14] E. F. Lambin and D. Ehrlich, "The surface temperature-vegetation index space for land cover and land-cover change analysis," *International Journal of Remote Sensing*, vol. 17, no. 3, pp. 463–487, 1996.

[15] Q. K. Hassan, C. P. A. Bourque, F. R. Meng, and W. Richards, "Spatial mapping of growing degree days: an application of MODIS-based surface temperatures and enhanced vegetation index," *Journal of Applied Remote Sensing*, vol. 1, no. 1, Article ID 013511, 2007.

[16] R. Nemani, L. Pierce, S. Running, and S. Goward, "Developing satellite-derived estimates of surface moisture status," *Journal of Applied Meteorology*, vol. 32, no. 3, pp. 548–557, 1993.

[17] D. Sun and M. Kafatos, "Note on the NDVI-LST relationship and the use of temperature-related drought indices over North America," *Geophysical Research Letters*, vol. 34, no. 24, Article ID L24406, 2007.

[18] Z. Sun, Q. Wang, B. Matsushita, T. Fukushima, Z. Ouyang, and M. Watanabe, "A new method to define the VI-Ts diagram using subpixel vegetation and soil information: a case study over a semiarid agricultural region in the North China plain," *Sensors*, vol. 8, no. 10, pp. 6260–6279, 2008.

[19] L. Jiang and S. Islam, "Estimation of surface evaporation map over Southern Great Plains using remote sensing data," *Water Resources Research*, vol. 37, no. 2, pp. 329–340, 2001.

[20] J. D. Kalma, T. R. McVicar, and M. F. McCabe, "Estimating land surface evaporation: a review of methods using remotely sensed surface temperature data," *Surveys in Geophysics*, vol. 29, no. 4-5, pp. 421–469, 2008.

[21] C. H. B. Priestley and R. J. Taylor, "On the assessment of surface heat flux and evaporation using large-scale parameters," *Monthly Weather Review*, vol. 100, no. 2, pp. 81–92, 1972.

[22] L. Jiang and S. Islam, "An intercomparison of regional latent heat flux estimation using remote sensing data," *International Journal of Remote Sensing*, vol. 24, no. 11, pp. 2221–2236, 2003.

[23] V. Venturini, G. Bisht, S. Islam, and L. Jiang, "Comparison of evaporative fractions estimated from AVHRR and MODIS sensors over South Florida," *Remote Sensing of Environment*, vol. 93, no. 1-2, pp. 77–86, 2004.

[24] K. Wang, Z. Li, and M. Cribb, "Estimation of evaporative fraction from a combination of day and night land surface temperatures and NDVI: a new method to determine the Priestley-Taylor parameter," *Remote Sensing of Environment*, vol. 102, no. 3-4, pp. 293–305, 2006.

[25] R. Tang, Z.-L. Li, and B. Tang, "An application of the Ts-VI triangle method with enhanced edges determination for evapotranspiration estimation from MODIS data in arid and semi-arid regions: implementation and validation," *Remote Sensing of Environment*, vol. 114, no. 3, pp. 540–551, 2010.

[26] Z.-L. Li, R. Tang, Z. Wan et al., "A review of current methodologies for regional evapotranspiration estimation from remotely sensed data," *Sensors*, vol. 9, no. 5, pp. 3801–3853, 2009.

[27] A. E. Lipton and J. M. Ward, "Satellite-view biases in retrieved surface temperatures in mountain areas," *Remote Sensing of Environment*, vol. 60, no. 1, pp. 92–100, 1997.

[28] Y. Gao, D. Long, and Z.-L. Li, "Estimation of daily actual evapotranspiration from remotely sensed data under complex terrain over the upper Chao river basin in North China," *International Journal of Remote Sensing*, vol. 29, no. 11, pp. 3295–3315, 2008.

[29] M. S. Moran, R. D. Jackson, L. H. Raymond, L. W. Gay, and P. N. Slater, "Mapping surface energy balance components by combining Landsat Thematic Mapper and ground-based meteorological data," *Remote Sensing of Environment*, vol. 30, no. 1, pp. 77–87, 1989.

[30] B. Matsushita, W. Yang, J. Chen, Y. Onda, and G. Qiu, "Sensitivity of the Enhanced Vegetation Index (EVI) and Normalized Difference Vegetation Index (NDVI) to topographic effects: a case study in high-density cypress forest," *Sensors*, vol. 7, no. 11, pp. 2636–2651, 2007.

[31] Y. Liu, T. Hiyama, and Y. Yamaguchi, "Scaling of land surface temperature using satellite data: a case examination on ASTER and MODIS products over a heterogeneous terrain area," *Remote Sensing of Environment*, vol. 105, no. 2, pp. 115–128, 2006.

[32] Z. Wan, *MODIS Land-Surface Temperature Algorithm Theoretical Basis Document (LST ATBD)*, Institute for Computational Earth System Science, Santa Barbara, Calif, USA, 1999.

[33] R. Richter, T. Kellenberger, and H. Kaufmann, "Comparison of topographic correction methods," *Remote Sensing*, vol. 1, no. 3, pp. 184–196, 2009.

[34] S. Liang, *Quantitative Remote Sensing of Land Surfaces*, Wiley-IEEE Press, New York, NY, USA, 2004.

[35] A. J. Prata, "A new long-wave formula for estimating downward clear-sky radiation at the surface," *Quarterly Journal of the Royal Meteorological Society*, vol. 122, no. 533, pp. 1127–1151, 1996.

[36] R. G. Keys, "Cubic convolution interpolation for digital image processing," *IEEE Transactions on Acoustics, Speech, and Signal Processing*, vol. 29, no. 6, pp. 1153–1160, 1981.

[37] S. A. Soenen, D. R. Peddle, and C. A. Coburn, "SCS+C: a modified sun-canopy-sensor topographic correction in forested terrain," *IEEE Transactions on Geoscience and Remote Sensing*, vol. 43, no. 9, pp. 2148–2159, 2005.

[38] H. Huang, P. Gong, N. Clinton, and F. Hui, "Reduction of atmospheric and topographic effect on Landsat TM data for forest classification," *International Journal of Remote Sensing*, vol. 29, no. 19, pp. 5623–5642, 2008.

[39] L. Blesius and F. Weirich, "The use of the Minnaert correction for land-cover classification in mountainous terrain," *International Journal of Remote Sensing*, vol. 26, no. 17, pp. 3831–3851, 2005.

[40] J. Wen, Q. Liu, Q. Liu, Q. Xiao, and X. Li, "Parametrized BRDF for atmospheric and topographic correction and albedo estimation in Jiangxi rugged terrain, China," *International Journal of Remote Sensing*, vol. 30, no. 11, pp. 2875–2896, 2009.

[41] S. A. Margulis, J. Kim, and T. Hogue, "A comparison of the triangle retrieval and variational data assimilation methods for surface turbulent flux estimation," *Journal of Hydrometeorology*, vol. 6, no. 6, pp. 1063–1072, 2005.

[42] Y. Liu, Y. Noumi, and Y. Yamaguchi, "Discrepancy between ASTER- and MODIS- derived land surface temperatures: terrain effects," *Sensors*, vol. 9, no. 2, pp. 1054–1066, 2009.

[43] D. Long, Y. Gao, and V. P. Singh, "Estimation of daily average net radiation from MODIS data and DEM over the Baiyangdian watershed in North China for clear sky days," *Journal of Hydrology*, vol. 388, no. 3-4, pp. 217–233, 2010.

[44] Y. Gao and W. Zhang, "A simple empirical topographic correction method for ETM+ imagery," *International Journal of Remote Sensing*, vol. 30, no. 9, pp. 2259–2275, 2009.

[45] Z. Zhang, R. R. De Wulf, F. M. B. Van Coillie, L. P. C. Verbeke, E. M. De Clercq, and X. Ou, "Influence of different topographic correction strategies on mountain vegetation classification accuracy in the Lancang Watershed, China," *Journal of Applied Remote Sensing*, vol. 5, no. 1, Article ID 053512, 2011.

[46] C. Aguilar, J. Herrero, and M. J. Polo, "Topographic effects on solar radiation distribution in mountainous watersheds and their influence on reference evapotranspiration estimates at watershed scale," *Hydrology and Earth System Sciences*, vol. 14, no. 12, pp. 2479–2494, 2010.

[47] S. Niemelä, P. Räisänen, and H. Savijärvi, "Comparison of surface radiative flux parameterizations part I: longwave radiation," *Atmospheric Research*, vol. 58, no. 1, pp. 1–18, 2001.

[48] J. Zillman, "A study of some aspects of the radiation and heat budgets of the southern hemisphere oceans," *Meteorological Studies*, no. 26, 562 pages, 1972.

[49] G. Bisht, V. Venturini, S. Islam, and L. Jiang, "Estimation of the net radiation using MODIS (Moderate Resolution Imaging Spectroradiometer) data for clear sky days," *Remote Sensing of Environment*, vol. 97, no. 1, pp. 52–67, 2005.

[50] J. P. Lagouarde and Y. Brunet, "A simple model for estimating the daily upward longwave surface radiation flux from NOAA-AVHRR data," *International Journal of Remote Sensing*, vol. 14, no. 5, pp. 907–925, 1993.